Evolution of Oxygen Ligands upon Large Redox Swings of Li_3IrO_4

Haifeng Li[1], Arnaud J. Perez[2,3], Beata Taudul[4,7], Teak D. Boyko[5], John W. Freeland[6], Marie-Liesse Doublet[4,7], Jean-Marie Tarascon[2,3,7], Jordi Cabana[1]

[1]Department of Chemistry, University of Illinois at Chicago, Chicago, Illinois 60607, United States

[2]Collège de France, Chimie du Solide et de l'Energie, UMR 8260, 11 Place Marcelin Berthelot, 75231 Paris Cedex 05, France

[3]Sorbonne Université, 4 Place Jussieu, F-75005 Paris, France

[4]ICGM, Univ Montpellier, CNRS, ENSCM, Montpellier, France

[5]Canadian Light Source, Saskatoon, Saskatchewan, S7N 2V3, Canada

[6]Advanced Photon Source, Argonne National Laboratory, Lemont, Illinois 60439, United States

[7]Réseau sur le Stockage Electrochimique de l'Energie (RS2E) CNRS FR3459, 33 rue Saint Leu, 80039 Amiens Cedex, France

Abstract

The limits of intercalation electrochemistry continue to be tested in the quest for ever increasing gains in the storage capability of Li-ion cathodes. The subsequent push for multi-electron reactivity has led to the recognition of the extremely versatile role of oxide ligands in charge compensation when there is a large redox swing. Li_3IrO_4 is a unique model of such activity because it can reversibly cycle between Li_1IrO_4 and $Li_{4.7}IrO_4$. Here, X-ray spectroscopy, magnetic measurements and computational simulations uncover the evolution of O states in the different steps, compared to the involvement of Ir. While the process between Li_1IrO_4 and Li_3IrO_4 is dominated by the unconventional lattice oxygen redox, the process between Li_3IrO_4 and $Li_{4.7}IrO_4$ involves a conventional change of the formal oxidation state of Ir, which affects O due to the high covalency. The O states of Li_3IrO_4 exhibit a very high reversibility after the whole 3.7-electron process, completely restoring the pristine state.

1. Introduction

As the world is transitioning into a clean energy paradigm and mobility that is free of emissions, energy storage has grown to be significantly prominent at a societal level.[1-5] Among energy storage devices, Li-ion batteries are the most promising due to their high energy density. The manipulation of the redox chemistry of the transition metal (TM)-oxide bond in reactions of electrochemical intercalation in solids was foundational to the advent of this technology. The storage process of the most widely used cathode, α-$NaFeO_2$-type layered transition metal oxides Li[TM]O_2 (TM = Co, Ni, Mn, among others), involves (de)intercalation concurrent with a conventional redox mechanism: $LiTM^{3+}O_2 \leftrightarrow xLi^+ + xe^- + Li_{(1-x)}TM^{(3+x)+}O_2$.[6] Challenges associated with the structural and chemical damage upon achieving high degrees of oxidation in these phases,[1, 7-9] have motivated researchers to define the limits of intercalation reactions to enable the largest possible reversible swings in composition and redox compensation.[3] In particular, a fundamental topic of interest is whether more than 1 mol Li can be stored per mol of total transition metal content.

In comparison with conventional layered oxides Li[TM]O_2, layered oxides with a Li overstoichiometry, Li[Li_xTM_{1-x}]O_2, have recently become the object of scrutiny due to the potential to achieve capacities as high as 300 $mAhg^{-1}$.[10-19] As a result, they seemingly break the barrier of 1 mol Li extracted per mol TM. This extraordinary activity stems from the accumulative contribution of conventional transition metal redox and O participation. Broadly speaking, unconventional ligand-centered redox (also referred to as “lattice oxygen redox”) is triggered in oxides as the stoichiometric ratio of oxide and transition metal increases,[20] and non-bonding states are incentivized in O by the existence of Li overstoichiometric in its coordination sphere.[21] Despite their enhanced electrochemical activity, they still suffer from detrimental chemical behavior, such

as oxygen evolution from the lattice,[22-24] extensive structural reorganization,[25-27] significant voltage hysteresis and fade,[28-30] and sluggish kinetics.[16, 31, 32]

In the quest to explore the fundamental limits of redox swing possible in an oxide, Perez et al. discovered that Li_3IrO_4 is capable of reversibly releasing Li at ~4 V vs. Li^+/Li^0 to form the nominal composition of Li_1IrO_4, while also uptaking Li down to 1.3 V to form nominally $Li_{4.7}IrO_4$.[33] The two processes could be combined in a single electrochemical experiment, for a total reversible swing of 3.7 mol Li per mol compound, the largest change observed in an oxide, even when compared to other Li_3TMO_4 phases.[34-37] This reactivity is thought to be enabled by the ability of oxide ligands to not only compensate changes in the formal charge of Ir, following conventional cation redox, but also to contribute electrons from initially non-bonding states that subsequently hybridize with Ir, such that the metal does not formally change charge.[33, 38]

Whereas *operando* Ir L_{III}-edge X-ray absorption spectroscopy (XAS) has been employed to study the electrochemical process between Li_1IrO_4 and $Li_{4.7}IrO_4$,[33] the detailed charge compensation mechanism must be completed by understanding the participation of O in the covalent interactions that enable it. The study of the Li_3IrO_4-Li_1IrO_4 revealed the existence of selective activity of the non-bonding states of the two unique O sites in the structure.[38] Here, we evaluate the changes occurring at O states in the complete compositional space, with a focus on whether the most reduced state, $Li_{4.7}IrO_4$, is the same if produced from Li_1IrO_4, after one initial charge, or directly upon reduction of Li_3IrO_4. To avoid confounding phenomena occurring at the surface of the materials,[27, 39, 40] we turn to O K-edge XAS with sensitivity to the interior of the material,[23, 24, 34, 41-46] complemented with magnetic measurements. The results complete the picture of the role of oxygen in the charge compensation mechanism in such a wide redox space.

2. Experimental and Computational Methods

2.1 Sample Preparation

Li_3IrO_4 was synthesized by a solid-state reaction of Li_2CO_3 (Sigma Aldrich, 99%) and metallic Ir (Alfa Aesar, 325 mesh, 99.9%) in stoichiometric proportions, as reported by the previous report.[33] The precursors were ground together using a mortar and pestle and then the homogeneous mixture was heated at 950°C for 24 hours in air atmosphere. After cooling to room temperature naturally, the as-synthesized sample was ground into fine powders and stored in an argon-filled glovebox (H_2O, O_2 < 0.1 ppm) for further characterization.

2.2 Working electrode preparation

Samples for *ex situ* XAS were prepared by galvanostatically cycling the positive electrode in typical two-electrode 2032 coin-type cells. The composite positive electrode materials were prepared by homogeneously mixing 80 wt% active material, 10 wt% carbon black (Denka), and 10 wt% polyvinylidene fluoride (PVDF) (Kynar) in 1-methyl-2-pyrrolidone (NMP, Sigma−Aldrich). The slurry were then blade-rolled on an electrochemically grade aluminum foil with the thickness of 6 mm and the typical active material loadings of 3-5 mg/cm^2, followed by a complete drying under vacuum at 110°C overnight. Dried electrodes were then punched into ½-inch diameter discs and transferred into an argon-filled glovebox (< 0.1 ppm of both H_2O and O_2) for further cell assembling. All the cells were fabricated in an argon-filled glove box with moisture and oxygen levels lower than 0.1 ppm. The cell was composed of the positive electrode and a high-purity lithium foil (Alfa Aesar) as the counter/reference electrode, separated by a 25-μm-thick polypropylene membrane (Celgard 2400), impregnated with 1 M $LiPF_6$ dissolved in a mixture of ethylene carbonate (EC)/dimethyl carbonate (DMC) (ethyl methyl carbonate (EMC) (3:7, wt %/ wt %). The galvanostatic charge–discharge cycling was performed at room temperature using a

BT-Lab tester with a current rate of C/20 (indicating 1 Li is extracted in 20 h) with cutoff voltages of interest. All potentials quoted in this paper were referenced to Li^+/Li^0 unless otherwise mentioned. Upon arriving at the state of interest, the cell was immediately stopped and disassembled in the argon-filled glovebox to avoid self-discharging under open-circuit state and the inside cycled electrode was harvested and washed with DMC three times, followed by drying under vacuum in the glovebox antechamber for 30 mins. Cleanly washed and dried electrodes were stored in the argon-filled glovebox for *ex situ* characterization.

Samples for *ex situ* magnetic measurements at different states of charge/discharge were prepared by cycling the pristine material in Swagelok-type cells. The active material was mixed with 10 wt% carbon SP and used as the positive electrode, while metallic lithium was used as the negative electrode. A Whatman GF/D borosilicate glass fiber membrane was used as the separator and was soaked with 1 M $LiPF_6$ in ethylene carbonate (EC)/propylene carbonate (PC)/dimethyl carbonate (DMC) with a volume ratio of 1:1:3. The cells were assembled in an argon-filled glovebox and galvanostatically cycled using VMP3 cycler at C/20 rate at room temperature. Once the state of interest was reached, the cell was disassembled in the glovebox and the material was harvested and washed using DMC, then dried under vacuum in the glovebox antechamber for 30 mins. Fully dried electrodes were stored in the argon-filled glovebox for characterization.

2.3 Magnetic measurements

Magnetic susceptibility measurements were carried out using a SQUID magnetometer (Quantum design), in zero field cooled (ZFC) mode, with an applied magnetic field of 1 kOe between 300 and 2 K. Samples were prepared by mixing with conductive carbon (Super C65 from Imerys, typical Fe content of 2 ppm), cycled at C/20 in Swagelok cell to the desired Li content and left to equilibrate for a few hours before recovering the powder, which was washed three times

with anhydrous dimethylcarbonate and dried under vacuum. About 10 to 20 mg of the samples were loaded into gel caps for the measurement and sealed in plastic tubes to avoid reaction with air prior to the measurement. The gel cap, plastic tube and conductive carbon were chosen for their negligible contribution to the magnetic susceptibility. The data was fitted between 25 and 250 K using a modified Curie-Weiss law with a temperature independent contribution χ_0 which takes into account the diamagnetic contribution of constituting diamagnetic elements (with an order of magnitude of -10^{-5} emu mol^{-1}):

$$\chi = \chi_0 + \frac{C}{T - \theta}$$

2.4 X-ray absorption spectroscopy

O K-edge X-ray absorption spectroscopy (XAS) data was collected *ex situ* at the beamline 4-ID-C of the Advance Photon Source (APS) at the Argonne National Laboratory. Samples of interest were attached to a 7T copper sample holder using conductive carbon tape in an argon-filled glovebox and then transferred into a 3-way transport container and then into an X-ray absorption antechamber through an argon environment to minimize the potential exposure to air. Data were measured simultaneously under both the total electron yield (TEY) mode from the sample photocurrent at ~10^{-9} Torr and total fluorescence yield (TFY) mode using a silicon drift diode detector (Vortex). Data was obtained at a spectral resolution of ~0.2 eV, with a 2 s dwell time. During the measurement, three scans were performed at each absorption edge, and scans were then averaged to maximize the signal-to-noise ratio. The energy scale of the spectra was calibrated with a Sr_2RuO_4 reference measured simultaneously with samples.

During the measurement, the XAS spectra were recorded over a wide energy range from 520 to 560 eV to cover energies well below and above sample absorptions. Then the normalization and

background removal were performed via established procedures in the literature.[47] First, the collected data was normalized to I_0 measured from the sample drain current from a freshly coated Au-mesh inserted into the beam path before the X-ray irradiates the sample. Subsequently, a linear, sloping background was removed from all spectra by fitting a linear function to the region from 520 to 524 eV, i.e. at energies below any absorption peaks.

2.5 DFT calculations

XAS simulation

The XAS spectra were computed for all structures using the OCEAN code[48, 49]OCEAN solves the Bethe-Salpeter equation (BSE)[50] based on the ground-state charge density and wave function obtained from the DFT-based Quantum Espresso (QE) program package,[51] using the local-density approximation (LDA or LDA+U)[52, 53] in conjunction with norm-conserving pseudopotentials.[54] To solve the Kohn-Sham equation, the cut-off value for the basis plane-waves was set to 952 eV and the k-point grid for the electronic density was converged with increasing k-point grids. As for VASP calculations used to relax all the structures prior to the XAS simulation, Hubbard correction was added to Ir(d) shell and spin-orbit coupling (SOC) was also considered to compute the electronic structures of materials. As shown in Figure S1, very similar electronic structures were obtained for Li_3IrO_4 and Li_4IrO_4 compounds when computed within the DFT+U formalism with or without including SOC. Remarkably, we observed that the splitting of the t_{2g} and e_g states reported as the origin of strong spin-orbit coupling in Ir-based oxides[55, 56] is already observed in the electronic structures obtained from DFT+U calculations and only slightly modified when SOC is further introduced. Accordingly, the influence of spin-orbit on the O K-edge XAS spectra is expected to be limited as the DFT+U formalism is used for the first-step electronic structure calculation on top of which the XAS simulation is performed.

The main advantage of the BSE approach is to explicitly account for the screened core-hole and photoelectron interaction and to include self-energy correction to the electronic states. In the present calculations, BSE was solved using 500 unoccupied bands and 800 bands were used to build the screened core-hole potential with the default k-point grid. Only dipole-allowed transitions were considered in the XAS calculations. The photon polarization vectors were set at [100], [010], and [001], and the final spectrum of each structure was obtained by averaging the spectra over all polarization vectors and individual oxygen atoms.

Core level shifts (CLS) were included in the calculations to account for the different local environment of the two oxygens occurring in the pristine Li_3IrO_4. The OCEAN code is built on top of one-electron wavefunction pseudopotentials with, in principle, no explicit access to core level states. To overcome this issue, OCEAN uses an optimal projection procedure[57] to orthogonalize the pseudized valence states to the core-states, alike the projected-augmented-wave (PAW) method developed by Blöchl[58] and used in VASP calculation. The relative shifts of the core-level energies are then evaluated through the change in the Kohn-Sham potential due to different chemical environments. Then the screening of the core-hole due to the valence electron, which also depends on the local environment of the absorbing atoms and on its charge, is computed through linear response theory. The convergence of the screening procedure was checked in our calculations by increasing the screening radius up to convergence. Absolute excitation energy were then aligned with the experimental data through an ad hoc shift.

3. Results and Discussion

The detailed electrochemical behavior and the corresponding verification of Li content in cycled samples have been reported in our previous publication.[33] Overall, Li can be directly intercalated into Li_3IrO_4 at low potential (black lines in Figure 1a), via a long plateau at ~1.7 V,

corresponding to a capacity equivalent to the insertion of 1.7 mol of Li per mol compound at 1.3 V. The subsequent oxidation to 2.5 V proceeds through two processes located at 1.8 and 1.9 V, respectively, leading to almost reversible re-extraction of 1.5 mol of Li. Ir L_{III}-edge XANES reveals significant, yet fully reversible changes in absorption energy associated with a conventional redox mechanism based on formal cationic centers, which reflects population of Ir 5d-O 2p covalent states. Li_3IrO_4 can also be oxidized to 4.5 V, resulting in the amorphization to "a-IrO_3" and an irreversible reduction to 2.0 V with notable voltage hysteresis and capacity loss (gray lines in Figure 1a). By limiting the initial oxidation to Li_1IrO_4, however, Li_3IrO_4 could experience a reversible subsequent reduction to 2.6 V with high reversibility.[33, 38] The compound can continue to be reduced to 1.3 V to produce an extraordinarily high capacity equivalent to 3.7 mol of Li per mol compound, followed by a reversible oxidation to the pristine state (Figure 1b). In order to study how and in what form O was involved in the electrochemical reactions, electrodes were harvested at representative state points of these electrochemical reactions, as indicated in Figure 1. This article combines data from XAS (Figure 2) and magnetic measurements (Figure 3), all of which probe the electronic structure centered at O 2p and Ir 5d states. Computational analysis probed the changes in electronic structure and quantitatively related them to the XAS.

O K-edge XAS is used to explore the variation of the electronic structure of O. Signals arise from dipole-allowed transition from core O *1s* to unoccupied O *2p* states. In general, the spectra of these transition metal compounds can be divided into two regions (Figures 2a). The pre-edge feature (≤ 535 eV, in general) represents the unoccupied states resulting from O *2p* orbitals hybridized with transition metal *nd* orbitals, and the broad band above 535 eV corresponds to a collection of excitations from O *1s* orbital to empty states of O *2p* orbitals mixed with the transition metal (n+1)*s* and (n+1)*p* orbitals, O 3*p* orbitals, and ultimately, the continuum. The position of the

pre-edge peak is affected by the change in the net electron density of the ligand via donating charge to the surrounding metal ion, the degree of d orbital splitting induced by the ligand field effect, and the overall *TM d*-manifold orbital energy.[59] The intensity of these peaks reflects both the density of unoccupied hybridized states and the degree of covalency of the ligand-metal bond.[60] In addition, the rising edge inflection point in the broad band deduced by the 1st derivative calculation of the XAS spectrum reflects the onset energy of the main edge position,[59] and thus could indicate the change in the binding energy of the O 1*s* core level.

The O K-edge XAS of pristine Li_3IrO_4 (Figures 2a) exhibits four distinct features centered at 527.9, 529.1, 531.7, and 533.7 eV, all below 535 eV, with the first three features corresponding to transitions to unoccupied O 2*p*-Ir 5*d* hybridized states, and the broad features above 535 eV arising from O 2*p*-Ir 6*s*, *p* states and the multiple scattering events upon photoionization. It should be noted that the small feature at 533.7 eV can be attributed to Li_2CO_3 impurity which dominates the surface signals (total electron yield, TEY, with a probing depth of 10 nm) (Figure 2a).[61] The result shows that these samples showed a notable sensitivity to air, with batches where contamination was enough to produce these signals, albeit at much lower relative intensity, even in fluorescence yield measurements (total fluorescence yield, TFY, with a penetration depth of 100 nm, probes the interior of the material, Figure 2b). Due to the presence of Li_2CO_3 and the potential for side reactions at the surface, the analysis mainly focused on TFY spectra to probe volumes where the bulk dominates the signal (Figure 2b). It is worthy of notice that spectral intensities in TFY are distorted by the self-absorption of fluorescent photons by the material, which is not present in TEY, so only qualitative trends between samples will be established.

In our previous paper, we reported that Li_3IrO_4 displays extremely reversible oxide-centered redox upon oxidation to Li_1IrO_4.[38] The following reduction was also possible, accumulating Li

beyond the initial state (sample F in Figure 1b).[33] O K-edge XAS of sample F ($Li_{3.6}IrO_4$) presented a shift of the first two pre-edge peaks to higher energy, at 528.1 and 529.1 eV, concurrent with a large decrease of their intensity (Figures 2b and S2), particularly at the lowest energy. These features are confirmed by DFT calculations for which a cationic reduction is predicted, consistent with a sharp decrease in intensity of the two peaks corresponding to the t_{2g}-like peaks supported by the projected density of states (pDOS) of Li_4IrO_4 which shows the decrease of a peak above Fermi level corresponding to the Ir d_{t2g}-O 2p states (Figures 4 and S3). Above 530 eV, the main feature at ~531.7 eV also experienced little shift to position, with an obvious, yet comparably smaller, reduction in intensity. Lastly, the rising absorption edge shifted to lower energy by ~0.2 eV compared to 2.6 V (Figure S4), indicating a relative decrease in the Z_{eff} of O and shallower binding energy shift.

Complete reduction to 1.3 V from Li_1IrO_4 induced a total swing of almost 4 mol of Li, and a nominal composition of $Li_{4.7}IrO_4$ (sample G in Figure 1b).[33] This sample was marked by an almost complete disappearance of pre-edge signals below 530 eV in the O K-edge XAS data, with the exception of a small, broad peak centered at 529.3 eV and little change above 530 eV compared to sample F (Figures 2b and S2), indicative of the consistency with changes in pDOS (Figure S3). The spectrum significantly broadened at higher energy, around the absorption edge, with a redshift of the inflection point by ~0.6 eV in comparison with the previous state (Figure S4).

The O K-edge XAS of the electrode harvested at 1.3 V after being charged to x = 1 (sample G) was almost perfectly equal to the spectrum of an electrode obtained by direct reduction of pristine Li_3IrO_4 to 1.3 V (sample J, Figures 2b, 2c and S2), further reinforcing the notion that the initial oxidation to Li_1IrO_4 is extremely reversible both from the electrochemical capacity and chemical perspectives. This reversibility is further demonstrated by the highly similar spectra of

pristine Li_3IrO_4 and the sample re-charged to 3 V after a full cycle of oxidation to x = 1 and reduction to 1.3 V (Figures 2b, 2d and S2). These observations emphasize the extremely high reversibility of the redox reaction between Li_1IrO_4 and $Li_{4.7}IrO_4$.

Significant evolution of the electronic structure between Li_3IrO_4 and $Li_{4.7}IrO_4$ upon lithiation is also reflected in magnetization data obtained on the samples directly reduced from the pristine state. The reduction process induced an increased paramagnetism from μ_{eff} = 0.82 μ_B/Ir in the pristine state (sample A, Li_3IrO_4, Figure 3a), to μ_{eff} = 1.46 μ_B/Ir for Li_4IrO_4 (sample I, Figure 3b). This value is close to reports for Ir^{4+} (d^5) compounds such as Li_2IrO_3 or Sr_2IrO_4 (1.7-2.0 μ_B/Ir).[62, 63] The magnetization of 5d materials, such as Ir compounds, is affected by the competition between spin-orbit coupling interaction and electron-electron correlation, the main consequence of which is lifting the degeneracy of the t_{2g} manifold into *effective* total angular momentum J_{eff} = 3/2 with low energy and J_{eff} = 1/2 with high energy. This is reflected in the weak paramagnetism (μ_{eff} = 0.2-0.9 μ_B/Ir) of Ir^{5+} (d^4) compounds, corresponding to four paired electrons in the J_{eff} = 3/2 levels and a J = 0 ground state, instead of the S = 1 ground state expected for a perfectly octahedral environment in the absence of spin-orbit coupling. In the case of Ir^{4+} (d^5) compounds, the J_{eff} = 3/2 level is filled, and one electron sits in the J_{eff} = ½ level, leading to a J = ½ ground state, thus explaining the increased moment found for Li_4IrO_4 compared to Li_3IrO_4. In contrast, further lithiation to $Li_{4.7}IrO_4$, obtained upon complete reduction to 1.3 V, corresponds to a decrease of μ_{eff} to 0.52 μ_B/Ir (Figure 3c). This observation is consistent with a large proportion of Ir^{3+} (d^6) with filled t_{2g} manifold (J_{eff} = 3/2 and ½), corresponding to a J = 0 ground state.[64, 65]

The changes below 3 V are accompanied by a steady shift of the Ir L_{III}-edge XANES to lower energy reported by Perez et al.[33] Therefore, the data support the injection of electrons into unoccupied O 2p-Ir 5d states following a conventional redox mechanism that can be explained by

changes in the formal oxidation state of Ir as a proxy for the Ir-O covalent bond. The pDOS (Figure S3) from DFT calculations clearly shows the decrease of a peak above Fermi level corresponding to the Ir d_{t2g}-O 2p states upon reduction, reflecting that electron mainly populated states arising from π interactions (t_{2g} in an ideal O_h field). This conclusion is further confirmed by the projection of calculated XAS on the two crystallographic oxygen sites (Figure S5) where the decrease in the two pre-edge peaks below 530 eV is due to the electron population of Ir d_{t2g}-O 2p states. The pre-edge peaks disappear completely after the composition reaches $Li_{4.5}IrO_4$ or higher. It should also be noted that after reaching the composition of Li_5IrO_4, the Ir d_{t2g}-O 2p states are filled and no longer observed above the Fermi level which is consistent with decrease in the pre-edge peaks in the experimental O K-edge XAS. It is possible that the smaller reduction of the pre-edge above 530 eV reflected a change in the contribution of O to the σ (e_g) states due to a decreased covalence of the Ir-O bond deduced by the simultaneous increase of Ir-O bond distance resulted from the accommodation of additional charge[33] (Table S1-1) and the calculated atomic Bader charge (Table S1-2). This distinct variation in the intensity reflects a greater role of unoccupied states at the lowest energy, in a behavior reminiscent of a rigid band. The redshift of the main absorption threshold indicates a decrease in the binding energy of the O 1*s* core level, consistent with re-population with electrons, and decrease in the Z_{eff} of O.

4. Conclusions

Li_3IrO_4 is capable of undergoing consecutive reactions based on unconventional lattice oxygen redox, between Li_1IrO_4 and Li_3IrO_4, followed by a transition to reach $Li_{4.7}IrO_4$ following a mechanism based on the changes of the formal oxidation state of Ir as a proxy for state with both Ir and O due to the high covalency. All along, O states participate in the redox compensation, with different involvement of Ir and, thus, different changes in electronic structure. Unlike the complex

changes between Li_1IrO_4 and Li_3IrO_4, the filling of states between Li_3IrO_4 and $Li_{4.7}IrO_4$ is highly reminiscent of a rigid model. Remarkably, the 3.7-electron whole process can be reversed completely to restore the pristine Li_3IrO_4. This report emphasizes the role of ligand oxygen in compensating the charge associated with (de)lithiation via manipulating its covalent interaction with transition metals. Should this manipulation be mimicked for oxides with 3d metals, combined processes of lattice oxygen redox and cationic redox could be achievable in a similarly sequential manner, resulting transformational amounts of charge storage in a single compound.

Acknowledgements

This material is based upon work supported by the National Science Foundation under Grant No. DMR-1809372. This research used resources of the Advanced Photon Source, a U.S. Department of Energy (DOE) Office of Science User Facility operated for the DOE Office of Science by Argonne National Laboratory under Contract No. DE-AC02-06CH11357. Part or all of the research described in this paper was performed at the Canadian Light Source, a national research facility of the University of Saskatchewan, which is supported by the Canada Foundation for Innovation (CFI), the Natural Sciences and Engineering Research Council (NSERC), the National Research Council (NRC), the Canadian Institutes of Health Research (CIHR), the Government of Saskatchewan, and the University of Saskatchewan.

Bibliography

1. Mizushima, K.; Jones, P. C.; Wiseman, P. J.; Goodenough, J. B., Li_xCoO_2 ($0<x<1$): A new cathode material for batteries of high energy density. *Mater. Res. Bull.* **1980,** 15, (6), 783-789.

2. Dunn, B.; Kamath, H.; Tarascon, J.-M., Electrical Energy Storage for the Grid: A Battery

of Choices. *Science* **2011,** 334, (6058), 928-935.

3. Whittingham, M. S., Ultimate Limits to Intercalation Reactions for Lithium Batteries. *Chem. Rev.* **2014,** 114, (23), 11414-11443.

4. Larcher, D.; Tarascon, J. M., Towards greener and more sustainable batteries for electrical energy storage. *Nat. Chem.* **2015,** 7, (1), 19-29.

5. Zubi, G.; Dufo-López, R.; Carvalho, M.; Pasaoglu, G., The lithium-ion battery: State of the art and future perspectives. *Renew. Sustain. Energy Rev.* **2018,** 89, 292-308.

6. Okubo, M.; Yamada, A., Molecular Orbital Principles of Oxygen-Redox Battery Electrodes. *ACS Appl. Mater. Interfaces* **2017,** 9, (42), 36463-36472.

7. Lu, Z.; MacNeil, D. D.; Dahn, J. R., Layered $Li[Ni_xCo_{1-2x}Mn_x]O_2$ Cathode Materials for Lithium-Ion Batteries. *Electrochem. Solid-State Lett.* **2001,** 4, (12), A200-A203.

8. Tsutomu, O.; Yoshinari, M., Layered Lithium Insertion Material of $LiCo_{1/3}Ni_{1/3}Mn_{1/3}O_2$ for Lithium-Ion Batteries. *Chem. Lett.* **2001,** 30, (7), 642-643.

9. Yoshizawa, H.; Ohzuku, T., An application of lithium cobalt nickel manganese oxide to high-power and high-energy density lithium-ion batteries. *J. Power Sources* **2007,** 174, (2), 813-817.

10. Lu, Z.; MacNeil, D. D.; Dahn, J. R., Layered Cathode Materials $Li[Ni_xLi_{1/3-2x/3}Mn_{2/3-x/3}]O_2$ for Lithium-Ion Batteries. *Electrochem. Solid-State Lett.* **2001,** 4, (11), A191.

11. Johnson, C. S.; Kim, J. S.; Lefief, C.; Li, N.; Vaughey, J. T.; Thackeray, M. M., The significance of the Li_2MnO_3 component in 'composite' $xLi_2MnO_3 \cdot (1-x)LiMn_{0.5}Ni_{0.5}O_2$ electrodes. *Electrochem. Commun.* **2004,** 6, (10), 1085-1091.

12. Thackeray, M. M.; Kang, S. H.; Johnson, C. S.; Vaughey, J. T.; Hackney, S. A., Comments on the structural complexity of lithium-rich $Li_{1+x}M_{1-x}O_2$ electrodes (M = Mn, Ni, Co) for lithium

batteries. *Electrochem. Commun.* **2006,** 8, (9), 1531-1538.

13. Thackeray, M. M.; Kang, S.-H.; Johnson, C. S.; Vaughey, J. T.; Benedek, R.; Hackney, S. A., Li_2MnO_3-stabilized $LiMO_2$ (M = Mn, Ni, Co) electrodes for lithium-ion batteries. *J. Mater. Chem.* **2007,** 17, (30), 3112.

14. Johnson, C. S.; Li, N.; Lefief, C.; Vaughey, J. T.; Thackeray, M. M., Synthesis, Characterization and Electrochemistry of Lithium Battery Electrodes: $xLi_2MnO_3 \cdot (1 - x)LiMn_{0.333}Ni_{0.333}Co_{0.333}O_2$ ($0 \leqslant x \leqslant 0.7$). *Chem. Mater. Chem. Mater.* **2008,** 20, (19), 6095-6106.

15. Rozier, P.; Tarascon, J. M., Review—Li-Rich Layered Oxide Cathodes for Next-Generation Li-Ion Batteries: Chances and Challenges. *J. Electrochem. Soc.* **2015,** 162, (14), A2490-A2499.

16. Assat, G.; Delacourt, C.; Corte, D. A. D.; Tarascon, J.-M., Editors' Choice—Practical Assessment of Anionic Redox in Li-Rich Layered Oxide Cathodes: A Mixed Blessing for High Energy Li-Ion Batteries. *J. Electrochem. Soc.* **2016,** 163, (14), A2965-A2976.

17. Redel, K.; Kulka, A.; Plewa, A.; Molenda, J., High-Performance Li-Rich Layered Transition Metal Oxide Cathode Materials for Li-Ion Batteries. *J. Electrochem. Soc.* **2019,** 166, (3), A5333-A5342.

18. Ates, M. N.; Mukerjee, S.; Abraham, K. M., A Li-Rich Layered Cathode Material with Enhanced Structural Stability and Rate Capability for Li-on Batteries. *J. Electrochem. Soc.* **2014,** 161, (3), A355-A363.

19. Penki, T. R.; Shanmughasundaram, D.; Kishore, B.; Jeyaseelan, A. V.; Subramani, A. K.; Munichandraiah, N., Composite of Li-Rich Mn, Ni and Fe Oxides as Positive Electrode Materials for Li-Ion Battery. *J. Electrochem. Soc.* **2016,** 163, (8), A1493-A1502.

20. Xie, Y.; Saubanère, M.; Doublet, M. L., Requirements for reversible extra-capacity in Li-

rich layered oxides for Li-ion batteries. *Energy Environ. Sci.* **2017,** 10, (1), 266-274.

21. Seo, D. H.; Lee, J.; Urban, A.; Malik, R.; Kang, S.; Ceder, G., The structural and chemical origin of the oxygen redox activity in layered and cation-disordered Li-excess cathode materials. *Nat. chem.* **2016,** 8, (7), 692-7.

22. Hong, J.; Lim, H.-D.; Lee, M.; Kim, S.-W.; Kim, H.; Oh, S.-T.; Chung, G.-C.; Kang, K., Critical Role of Oxygen Evolved from Layered Li–Excess Metal Oxides in Lithium Rechargeable Batteries. *Chem. Mater.* **2012,** 24, (14), 2692-2697.

23. Luo, K.; Roberts, M. R.; Guerrini, N.; Tapia-Ruiz, N.; Hao, R.; Massel, F.; Pickup, D. M.; Ramos, S.; Liu, Y.-S.; Guo, J.; Chadwick, A. V.; Duda, L. C.; Bruce, P. G., Anion Redox Chemistry in the Cobalt Free 3d Transition Metal Oxide Intercalation Electrode $Li[Li_{0.2}Ni_{0.2}Mn_{0.6}]O_2$. *J. Am. Chem. Soc.* **2016,** 138, (35), 11211-11218.

24. Luo, K.; Roberts, M. R.; Hao, R.; Guerrini, N.; Pickup, D. M.; Liu, Y. S.; Edstrom, K.; Guo, J.; Chadwick, A. V.; Duda, L. C.; Bruce, P. G., Charge-compensation in 3d-transition-metal-oxide intercalation cathodes through the generation of localized electron holes on oxygen. *Nat. Chem.* **2016,** 8, (7), 684-91.

25. Tran, N.; Croguennec, L.; Ménétrier, M.; Weill, F.; Biensan, P.; Jordy, C.; Delmas, C., Mechanisms Associated with the "Plateau" Observed at High Voltage for the Overlithiated $Li_{1.12}(Ni_{0.425}Mn_{0.425}Co_{0.15})_{0.88}O_2$ System. *Chem. Mater.* **2008,** 20, (15), 4815-4825.

26. Jiang, M.; Key, B.; Meng, Y. S.; Grey, C. P., Electrochemical and Structural Study of the Layered, "Li-Excess" Lithium-Ion Battery Electrode Material $Li[Li_{1/9}Ni_{1/3}Mn_{5/9}]O_2$. *Chem. Mater.* **2009,** 21, (13), 2733-2745.

27. Yabuuchi, N.; Yoshii, K.; Myung, S.-T.; Nakai, I.; Komaba, S., Detailed Studies of a High-Capacity Electrode Material for Rechargeable Batteries, Li_2MnO_3−$LiCo_{1/3}Ni_{1/3}Mn_{1/3}O_2$. *J. Am.*

Chem. Soc. **2011,** 133, (12), 4404-4419.

28. Croy, J. R.; Gallagher, K. G.; Balasubramanian, M.; Chen, Z.; Ren, Y.; Kim, D.; Kang, S.-H.; Dees, D. W.; Thackeray, M. M., Examining Hysteresis in Composite $xLi_2MnO_3 \cdot (1–x)LiMO_2$ Cathode Structures. *J. Phys. Chem. C* **2013,** 117, (13), 6525-6536.

29. Croy, J. R.; Gallagher, K. G.; Balasubramanian, M.; Long, B. R.; Thackeray, M. M., Quantifying Hysteresis and Voltage Fade in $xLi_2MnO_3 \bullet (1\text{-}x)LiMn_{0.5}Ni_{0.5}O_2$ Electrodes as a Function of Li_2MnO_3 Content. *J. Electrochem. Soc.* **2014,** 161, (3), A318-A325.

30. Jacquet, Q.; Iadecola, A.; Saubanère, M.; Li, H.; Berg, E. J.; Rousse, G.; Cabana, J.; Doublet, M.-L.; Tarascon, J.-M., Charge Transfer Band Gap as an Indicator of Hysteresis in Li-Disordered Rock Salt Cathodes for Li-Ion Batteries. *J. Am. Chem. Soc.* **2019,** 141, (29), 11452-11464.

31. Assat, G.; Foix, D.; Delacourt, C.; Iadecola, A.; Dedryvère, R.; Tarascon, J.-M., Fundamental interplay between anionic/cationic redox governing the kinetics and thermodynamics of lithium-rich cathodes. *Nat. Commun.* **2017,** 8, (1), 2219.

32. Assat, G.; Tarascon, J.-M., Fundamental understanding and practical challenges of anionic redox activity in Li-ion batteries. *Nat. Energy* **2018,** 3, (5), 373-386.

33. Perez, A. J.; Jacquet, Q.; Batuk, D.; Iadecola, A.; Saubanère, M.; Rousse, G.; Larcher, D.; Vezin, H.; Doublet, M.-L.; Tarascon, J.-M., Approaching the limits of cationic and anionic electrochemical activity with the Li-rich layered rocksalt Li_3IrO_4. *Nat. Energy* **2017,** 2, (12), 954-962.

34. Yabuuchi, N.; Takeuchi, M.; Nakayama, M.; Shiiba, H.; Ogawa, M.; Nakayama, K.; Ohta, T.; Endo, D.; Ozaki, T.; Inamasu, T.; Sato, K.; Komaba, S., High-capacity electrode materials for rechargeable lithium batteries: Li_3NbO_4-based system with cation-disordered rocksalt structure.

*Proc. Natl. Acad. Sci.***2015,** 112, (25), 7650-7655.

35. Jacquet, Q.; Perez, A.; Batuk, D.; Van Tendeloo, G.; Rousse, G.; Tarascon, J.-M., The $Li_3Ru_yNb_{1-y}O_4$ ($0 \leqslant y \leqslant 1$) System: Structural Diversity and Li Insertion and Extraction Capabilities. *Chem. Mater.* **2017,** 29, (12), 5331-5343.

36. Jacquet, Q.; Iadecola, A.; Saubanère, M.; Lemarquis, L.; Berg, E. J.; Alves Dalla Corte, D.; Rousse, G.; Doublet, M.-L.; Tarascon, J.-M., Competition between Metal Dissolution and Gas Release in Li-Rich $Li_3Ru_yIr_{1-y}O_4$ Model Compounds Showing Anionic Redox. *Chem. Mater.* **2018,** 30, (21), 7682-7690.

37. Li, H.; Ramakrishnan, S.; Freeland, J. W.; McCloskey, B. D.; Cabana, J., Definition of Redox Centers in Reactions of Lithium Intercalation in Li_3RuO_4 Polymorphs. *J. Am. Chem. Soc.* **2020,** 142, (18), 8160-8173.

38. Li, H.; Perez, A. J.; Taudul, B.; Boyko, T. D.; Freeland, J. W.; Doublet, M.-L.; Tarascon, J.-M.; Cabana, J., Elucidation of Active Oxygen Sites upon Delithiation of Li_3IrO_4. *ACS Energy Lett.* **2021,** 6, (1), 140-147.

39. Koga, H.; Croguennec, L.; Ménétrier, M.; Mannessiez, P.; Weill, F.; Delmas, C., Different oxygen redox participation for bulk and surface: A possible global explanation for the cycling mechanism of $Li_{1.20}Mn_{0.54}Co_{0.13}Ni_{0.13}O_2$. *J. Power Sources* **2013,** 236, 250-258.

40. Yan, P.; Nie, A.; Zheng, J.; Zhou, Y.; Lu, D.; Zhang, X.; Xu, R.; Belharouak, I.; Zu, X.; Xiao, J.; Amine, K.; Liu, J.; Gao, F.; Shahbazian-Yassar, R.; Zhang, J.-G.; Wang, C.-M., Evolution of Lattice Structure and Chemical Composition of the Surface Reconstruction Layer in $Li_{1.2}Ni_{0.2}Mn_{0.6}O_2$ Cathode Material for Lithium Ion Batteries. *Nano Lett.* **2015,** 15, (1), 514-522.

41. Hy, S.; Su, W.-N.; Chen, J.-M.; Hwang, B.-J., Soft X-ray Absorption Spectroscopic and Raman Studies on $Li_{1.2}Ni_{0.2}Mn_{0.6}O_2$ for Lithium-Ion Batteries. *J. Phys. Chem. C* **2012,** 116, (48),

25242-25247.

42. Oishi, M.; Fujimoto, T.; Takanashi, Y.; Orikasa, Y.; Kawamura, A.; Ina, T.; Yamashige, H.; Takamatsu, D.; Sato, K.; Murayama, H.; Tanida, H.; Arai, H.; Ishii, H.; Yogi, C.; Watanabe, I.; Ohta, T.; Mineshige, A.; Uchimoto, Y.; Ogumi, Z., Charge compensation mechanisms in $Li_{1.16}Ni_{0.15}Co_{0.19}Mn_{0.50}O_2$ positive electrode material for Li-ion batteries analyzed by a combination of hard and soft X-ray absorption near edge structure. *J. Power Sources* **2013,** 222, 45-51.

43. Oishi, M.; Yamanaka, K.; Watanabe, I.; Shimoda, K.; Matsunaga, T.; Arai, H.; Ukyo, Y.; Uchimoto, Y.; Ogumi, Z.; Ohta, T., Direct observation of reversible oxygen anion redox reaction in Li-rich manganese oxide, , Li_2MnO_3, studied by soft X-ray absorption spectroscopy. *J. Mater. Chem. A* **2016,** 4, (23), 9293-9302.

44. Mortemard de Boisse, B.; Liu, G.; Ma, J.; Nishimura, S.; Chung, S. C.; Kiuchi, H.; Harada, Y.; Kikkawa, J.; Kobayashi, Y.; Okubo, M.; Yamada, A., Intermediate honeycomb ordering to trigger oxygen redox chemistry in layered battery electrode. *Nat. Commun.* **2016,** 7, 11397.

45. Yabuuchi, N.; Nakayama, M.; Takeuchi, M.; Komaba, S.; Hashimoto, Y.; Mukai, T.; Shiiba, H.; Sato, K.; Kobayashi, Y.; Nakao, A.; Yonemura, M.; Yamanaka, K.; Mitsuhara, K.; Ohta, T., Origin of stabilization and destabilization in solid-state redox reaction of oxide ions for lithium-ion batteries. *Nat. Commun* **2016,** 7, (1), 13814.

46. Yang, W.; Devereaux, T. P., Anionic and cationic redox and interfaces in batteries: Advances from soft X-ray absorption spectroscopy to resonant inelastic scattering. *J. Power Sources* **2018,** 389, 188-197.

47. Stöhr, J., *NEXAFS Spectroscopy*. Springer: 1992.

48. Vinson, J.; Rehr, J. J.; Kas, J. J.; Shirley, E. L., Bethe-Salpeter equation calculations of

core excitation spectra. *Phys. Rev. B* **2011,** 83, (11), 115106.

49. Gilmore, K.; Vinson, J.; Shirley, E. L.; Prendergast, D.; Pemmaraju, C. D.; Kas, J. J.; Vila, F. D.; Rehr, J. J., Efficient implementation of core-excitation Bethe–Salpeter equation calculations. *Comput. Phys. Commun.* **2015,** 197, 109-117.

50. Salpeter, E. E.; Bethe, H. A., A Relativistic Equation for Bound-State Problems. *Phys. Rev.* **1951,** 84, (6), 1232-1242.

51. Giannozzi, P.; Baroni, S.; Bonini, N.; Calandra, M.; Car, R.; Cavazzoni, C.; Ceresoli, D.; Chiarotti, G. L.; Cococcioni, M.; Dabo, I.; Dal Corso, A.; de Gironcoli, S.; Fabris, S.; Fratesi, G.; Gebauer, R.; Gerstmann, U.; Gougoussis, C.; Kokalj, A.; Lazzeri, M.; Martin-Samos, L.; Marzari, N.; Mauri, F.; Mazzarello, R.; Paolini, S.; Pasquarello, A.; Paulatto, L.; Sbraccia, C.; Scandolo, S.; Sclauzero, G.; Seitsonen, A. P.; Smogunov, A.; Umari, P.; Wentzcovitch, R. M., QUANTUM ESPRESSO: a modular and open-source software project for quantum simulations of materials. *J. Phys.: Condens. Matter* **2009,** 21, (39), 395502.

52. Ceperley, D. M.; Alder, B. J., Ground State of the Electron Gas by a Stochastic Method. *Phys. Rev. Lett.* **1980,** 45, (7), 566-569.

53. Perdew, J. P.; Wang, Y., Accurate and simple analytic representation of the electron-gas correlation energy. *Phys. Rev. B* **1992,** 45, (23), 13244-13249.

54. Troullier, N.; Martins, J. L., Efficient pseudopotentials for plane-wave calculations. *Phys. Rev. B, Condens. Matter* **1991,** 43, (3), 1993-2006.

55. Clancy, J. P.; Chen, N.; Kim, C. Y.; Chen, W. F.; Plumb, K. W.; Jeon, B. C.; Noh, T. W.; Kim, Y.-J., Spin-orbit coupling in iridium-based 5d compounds probed by x-ray absorption spectroscopy. *Phys. Rev. B* **2012,** 86, (19), 195131.

56. Laguna-Marco, M. A.; Kayser, P.; Alonso, J. A.; Martínez-Lope, M. J.; van Veenendaal,

M.; Choi, Y.; Haskel, D., Electronic structure, local magnetism, and spin-orbit effects of Ir(IV)-, Ir(V)-, and Ir(VI)-based compounds. *Phys. Rev. B* **2015,** 91, (21), 214433.

57. Shirley, E. L., Local screening of a core hole: A real-space approach applied to hafnium oxide. *Ultramicroscopy* **2006,** 106, (11), 986-993.

58. Blöchl, P. E., Projector augmented-wave method. *Phys. Rev. B* **1994,** 50, (24), 17953-17979.

59. Shadle, S. E.; Hedman, B.; Hodgson, K. O.; Solomon, E. I., Ligand K-Edge X-ray Absorption Spectroscopy as a Probe of Ligand-Metal Bonding: Charge Donation and Covalency in Copper-Chloride Systems. *Inorg. Chem.* **1994,** 33, (19), 4235-4244.

60. Wasinger, E. C.; de Groot, F. M. F.; Hedman, B.; Hodgson, K. O.; Solomon, E. I., L-edge X-ray Absorption Spectroscopy of Non-Heme Iron Sites: Experimental Determination of Differential Orbital Covalency. *J. Am. Chem. Soc.* **2003,** 125, (42), 12894-12906.

61. Qiao, R.; Chuang, Y. D.; Yan, S.; Yang, W., Soft x-ray irradiation effects of Li_2O_2, Li_2CO_2 and Li_2O revealed by absorption spectroscopy. *PloS one* **2012,** 7, (11), e49182.

62. Winter, S. M.; Tsirlin, A. A.; Daghofer, M.; van den Brink, J.; Singh, Y.; Gegenwart, P.; Valentí, R., Models and materials for generalized Kitaev magnetism. *J. Phys.: Condens. Matter* **2017,** 29, (49), 493002.

63. Kim, B. J.; Jin, H.; Moon, S. J.; Kim, J. Y.; Park, B. G.; Leem, C. S.; Yu, J.; Noh, T. W.; Kim, C.; Oh, S. J.; Park, J. H.; Durairaj, V.; Cao, G.; Rotenberg, E., Novel J_{eff} = 1/2 Mott State Induced by Relativistic Spin-Orbit Coupling in Sr_2IrO_4. *Phys. Rev. Lett.***2008,** 101, (7), 076402.

64. Weber, D.; Schoop, L. M.; Wurmbrand, D.; Nuss, J.; Seibel, E. M.; Tafti, F. F.; Ji, H.; Cava, R. J.; Dinnebier, R. E.; Lotsch, B. V., Trivalent Iridium Oxides: Layered Triangular Lattice Iridate $K_{0.75}Na_{0.25}IrO_2$ and Oxyhydroxide IrOOH. *Chem. Mater.* **2017,** 29, (19), 8338-8345.

65. Page, J. E.; Hayward, M. A., $CaMn_{0.5}Ir_{0.5}O_{2.5}$: An Anion-Deficient Perovskite Oxide Containing Ir^{3+}. *Inorg. Chem.* **2019,** 58, (13), 8835-8840.

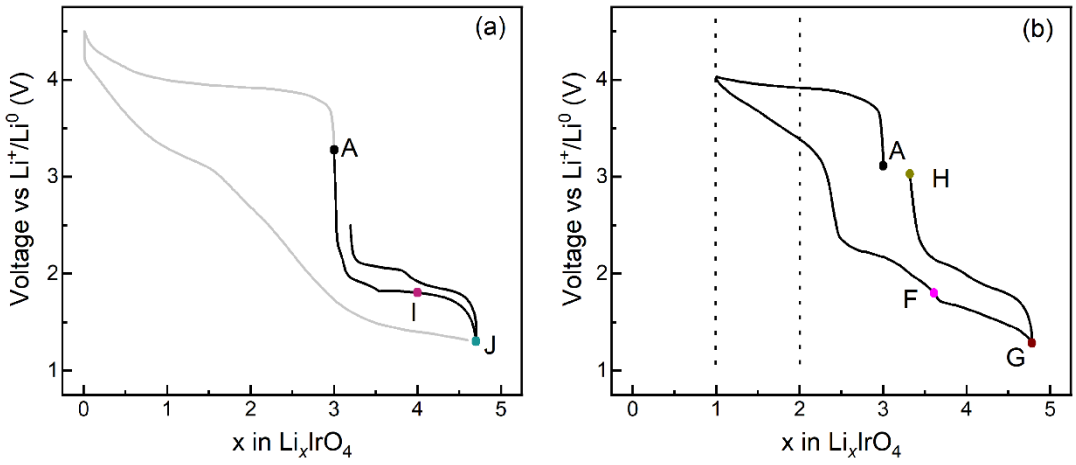

Figure 1. (a) and (b) Voltage-composition profiles of Li_3IrO_4 at different cutoff voltage windows. The electrochemical states of interest are represented with labels of different colors. Samples were harvested from the representative states. A is the pristine state. Cycled samples were obtained after initial oxidation to x = 1 and reduction to 1.8 V (F); reduction to 1.3 V (G); reduction to 1.3 V and re-oxidation to 3.0 V (H). Sample I was obtained by a direct reduction to x = 4 from the pristine state and sample J was obtained by a direction reduction to 1.3 V from the pristine state.

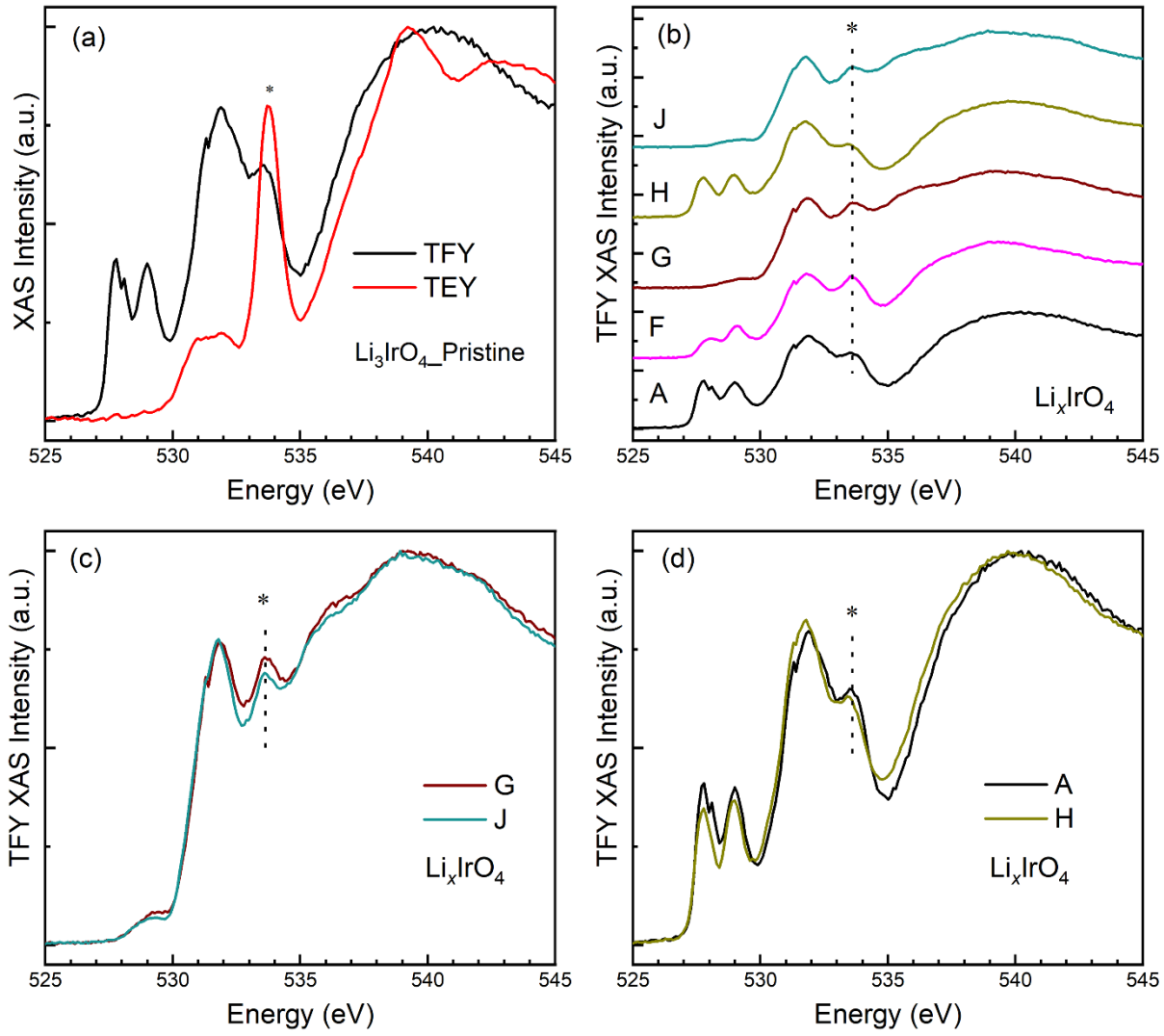

Figure 2. (a) O K-edge XAS spectra of Li_3IrO_4 pristine state measured under different modes. TFY: total fluorescence yield. TEY: total electron yield. The TFY spectrum is dominated by a peak at ~533.7 eV, which is attributed to the transition to π^* (C=O) orbitals in Li_2CO_3 impurity formed mainly in the surface.[61] The minor presence of Li_2CO_3-related peak in TFY also suggests some existence of Li_2CO_3 below the surface. Due to the significant existence of Li_2CO_3 in the surface through all different electrochemical states, O K-edge XAS spectra from TFY were the focus of our work. (b) *Ex situ* O 1*s* XAS spectra of Li_xIrO_4 at difference electrochemical states of charge measured under TFY mode. (c) and (d) Overlaid O 1*s* XAS spectra of sample G and sample

J, sample A and sample H, respectively. The peak at around 533.7 eV (denoted by the asterisk symbol) is related to carbonate-related peak due to the transitions to π^* (C=O) orbitals, which has little influence on the spectral interpretation.

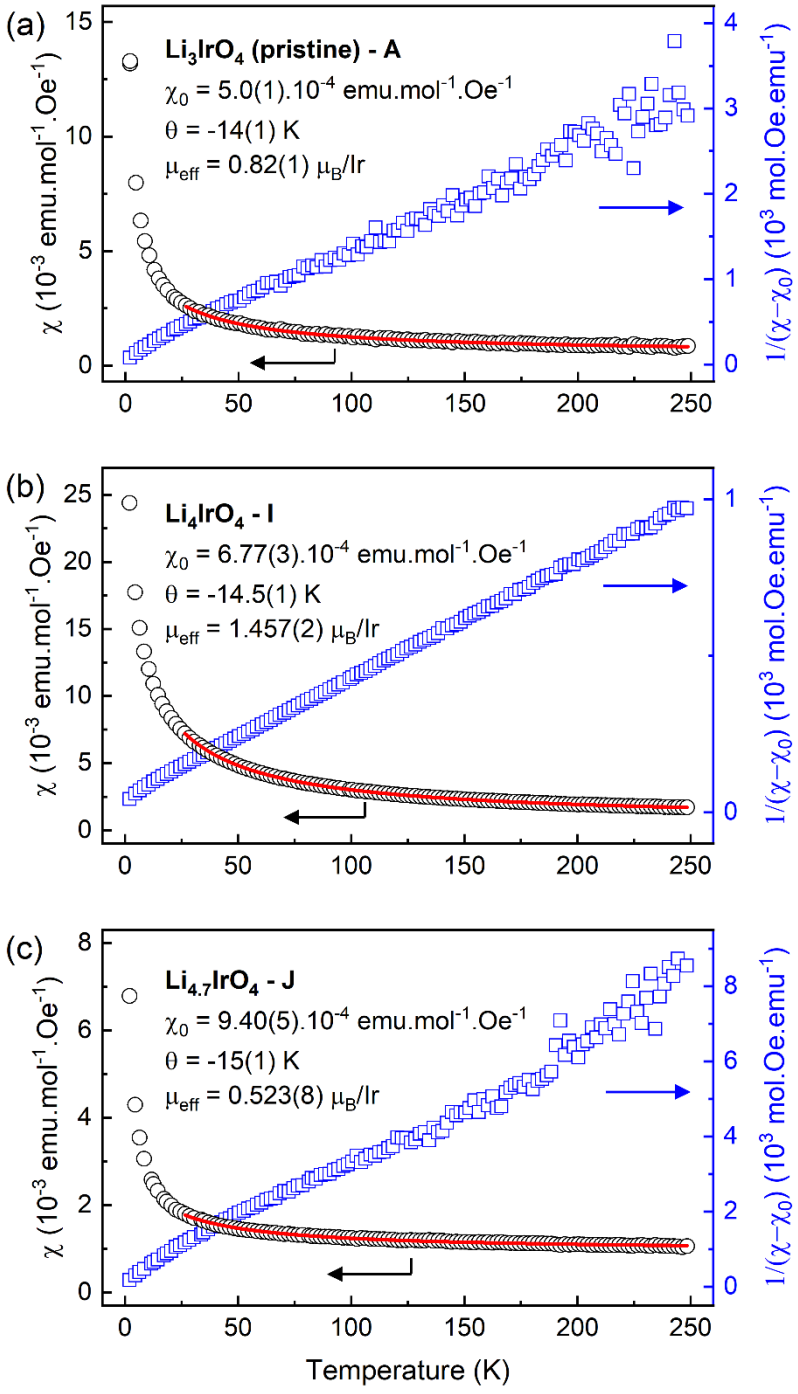

Figure 3. Magnetization measurement of Li_xIrO_4 with different Li contents at x = 3 (a), x = 4 (b), and x = 4.7 (c) was performed *ex situ*. The black circles are zero-field cooled magnetic susceptibility measurements, the red line is obtained from fitting the data with a modified Curie-Weiss law, with the fitting parameters indicated, and the blue circles are the inverse magnetic susceptibility after removing the temperature independent contribution χ_0.

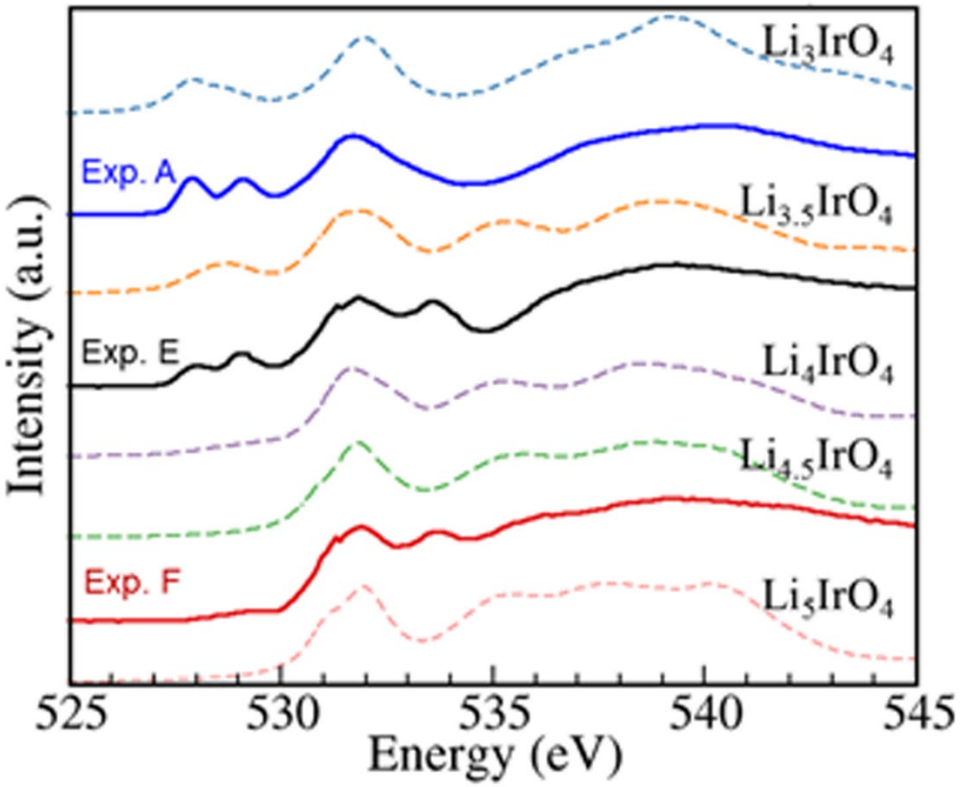

Figure 4. Simulated O K-edge XAS spectra of different electrochemical states and the corresponding experimental results. The XAS projected on the O_{3LP} and O_{2LP} absorbing species are shown in Figure S4. The peak at ~534 eV in the experimental data is ascribed to the presence of Li_2CO_3 impurities.

Supporting Information

Evolution of Oxygen Ligands upon Large Redox Swings of Li_3IrO_4

Haifeng Li[1], Arnaud J. Perez[2,3], Beata Taudul[4], Teak D. Boyko[5], John W. Freeland[6], Marie-Liesse Doublet[4], Jean-Marie Tarascon[2,3,7], Jordi Cabana[1]

[1]Department of Chemistry, University of Illinois at Chicago, Chicago, Illinois 60607, United States

[2]Collège de France, Chimie du Solide et de l'Energie, UMR 8260, 11 Place Marcelin Berthelot, 75231 Paris Cedex 05, France

[3]Sorbonne Université, 4 Place Jussieu, F-75005 Paris, France

[4]ICGM, Univ Montpellier, CNRS, ENSCM, Montpellier, France

[5]Canadian Light Source, Saskatoon, Saskatchewan, S7N 2V3, Canada

[6]Advanced Photon Source, Argonne National Laboratory, Lemont, Illinois 60439, United States

[7]Réseau sur le Stockage Electrochimique de l'Energie (RS2E) CNRS FR3459, 33 rue Saint Leu, 80039 Amiens Cedex, France

Supplementary Figures

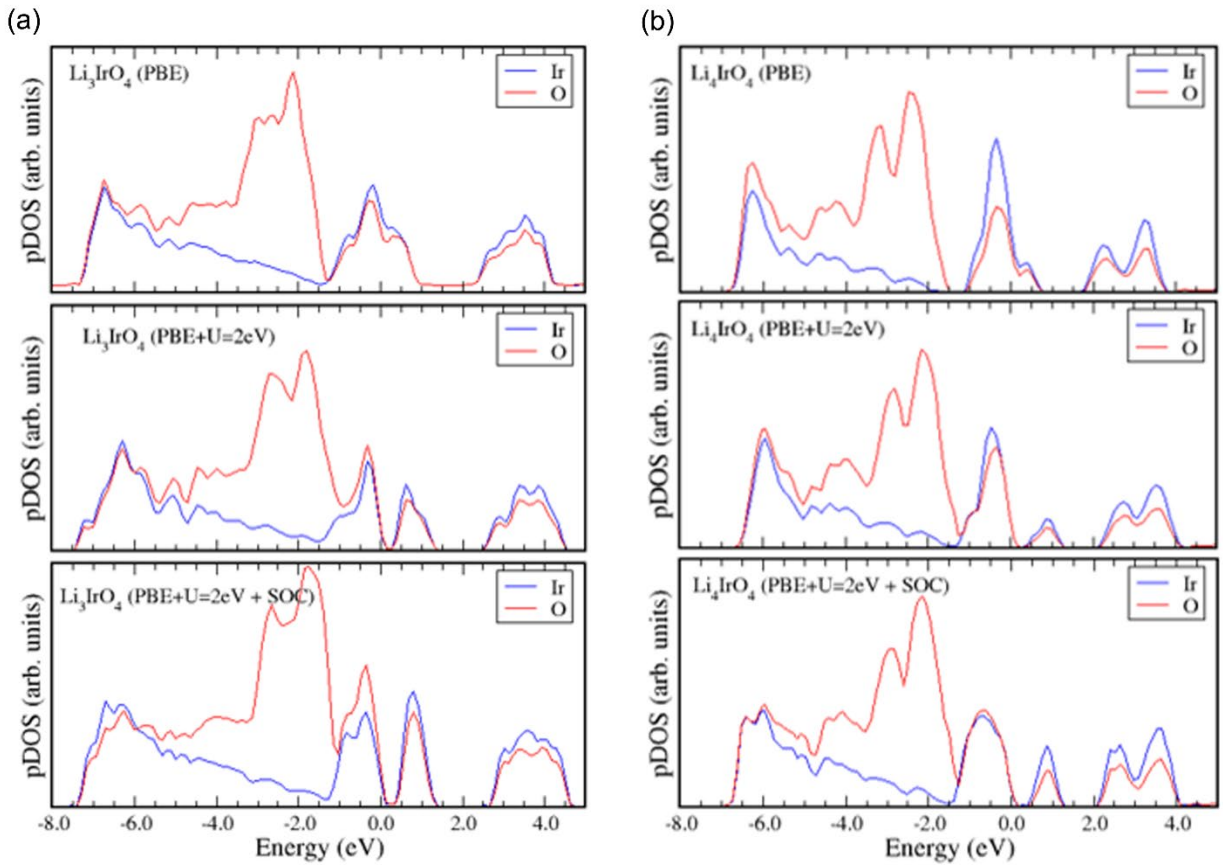

Figure S1. Atom-projected Density of States for (a) Li_3IrO_4 and (b) Li_3IrO_4, as computed with DFT (PBE), DFT+U and DFT+U+SOC formalisms (VASP code). As expected, conventional DFT fails in describing strongly correlated systems, such as transition metal oxides, and leads to an erroneous metallic ground state for Li_3IrO_4. In contrast, the DFT+U formalism, which partially corrects the self-interaction error of conventional DFT through the introduction of the on-site (d-shell) Hubbard coulombic parameter (U), leads to the expected Mott-Hubbard transition and to the splitting of the t_{2g} states. The amplitude of this splitting is only slightly affected when spin-orbit coupling (SOC) is added in the calculations, suggesting that the O K-edge spectra are not significantly affected by SOC effects on Ir.

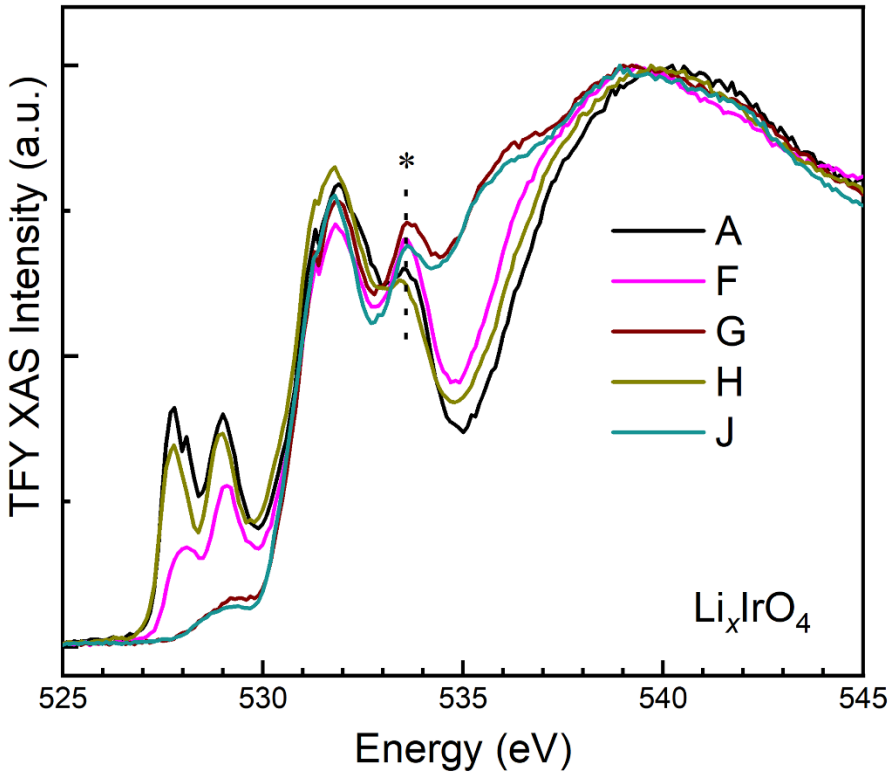

Figure S2. Overlaid O K-edge XAS spectra of Li_3IrO_4 at different states of charge.

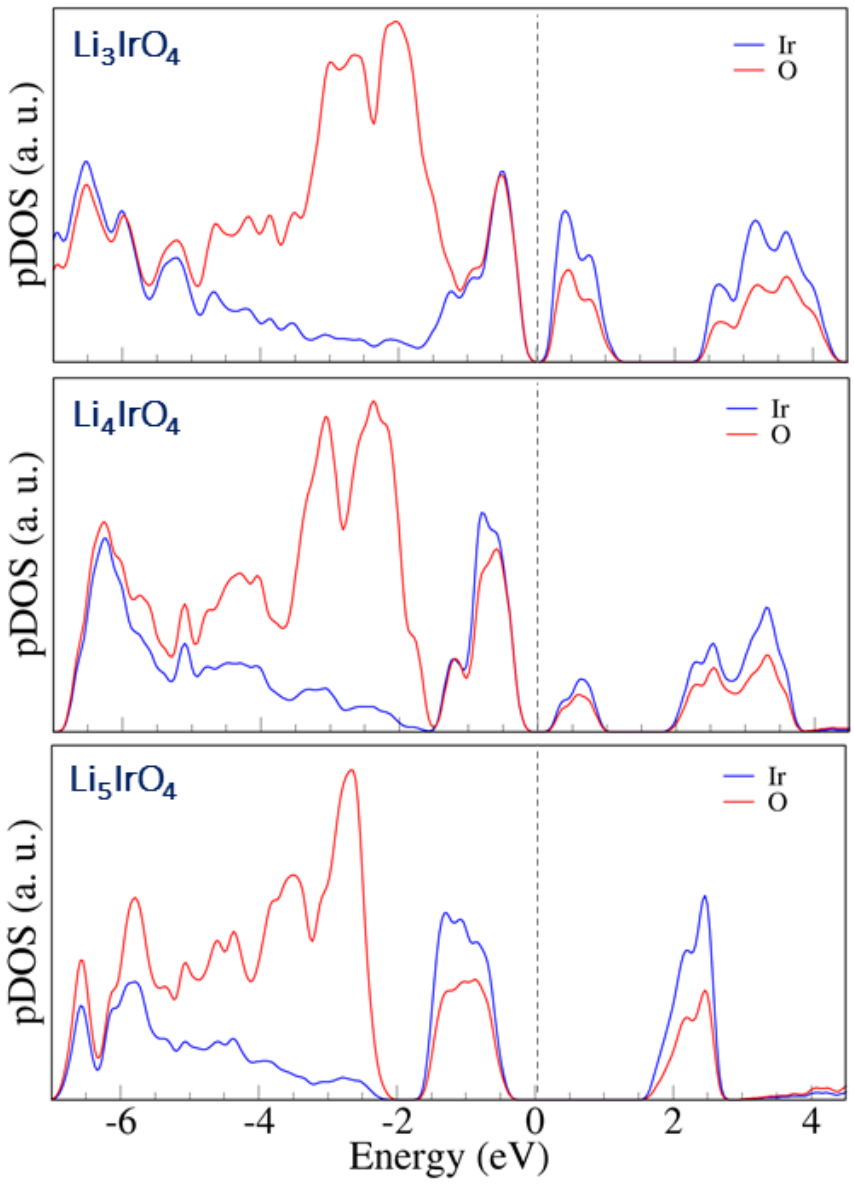

Figure S3. Projected density of states (pDOS) for Li_3IrO_4, Li_4IrO_4 and Li_5IrO_4 obtained for ordered phases with GGA plus U=2 eV Hubbard correction.

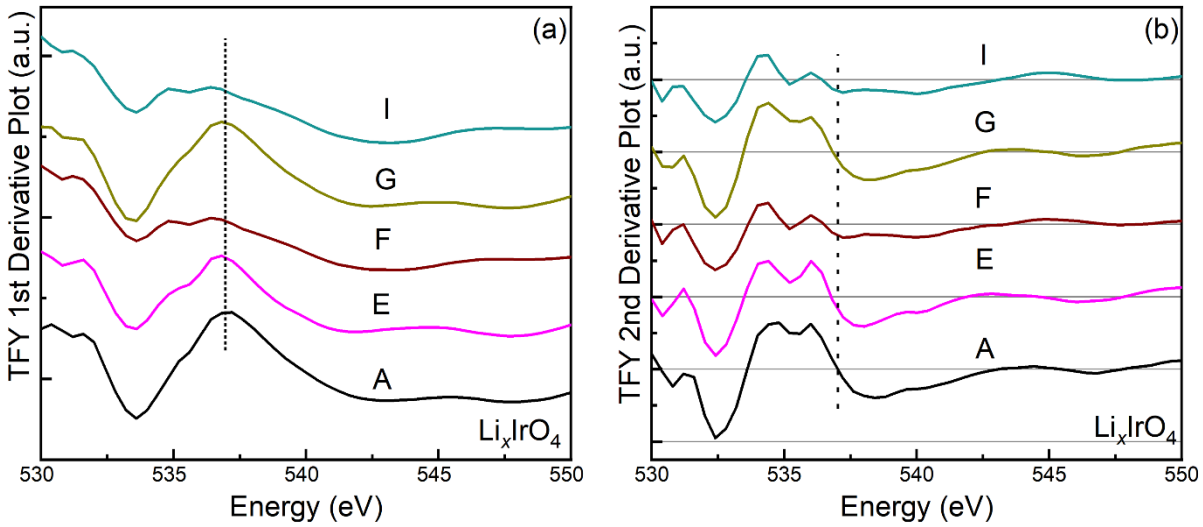

Figure S4. The first (a) and second derivative (b) plots of O K-edge XAS spectra of Li_3IrO_4 at different states of charge indicated in the electrochemical profile.

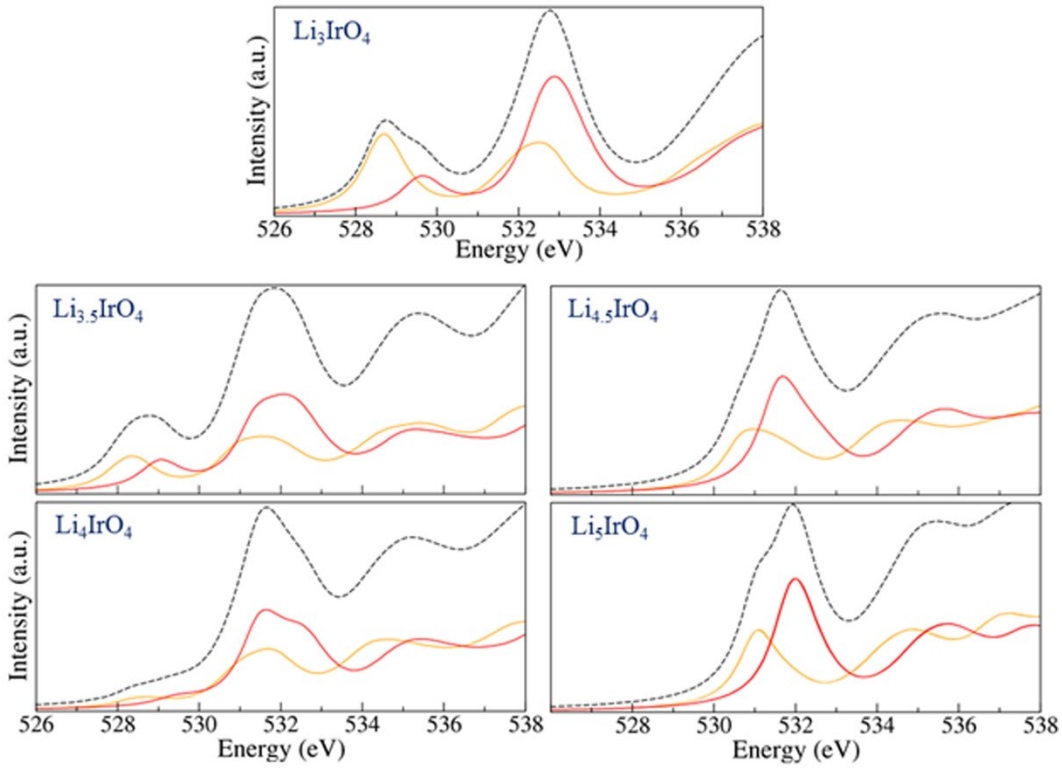

Figure S5. Simulated O K-edge XAS spectra projected on the different oxygen sites for different electrochemical state of discharge and the corresponding experimental results.

Table S1. Ir-O distance (S1-1) of different states of charge during the reduction based on DFT calculations and associated Ir and O atomic population (e^-) and Bader charges (S1-2). Note that, at intermediate Li compositions 3.5 and 4.5, the occurrence of two Ir with different Bader charges arises from the Li/vacancy order chosen in the calculations.

Table S1-1. Ir-O distance						
	Ir1-O1 (Å)	Ir1-O3 (Å)	Ir1-O8 (Å)	Ir1-O7 (Å)	Ir1-O5 (Å)	Ir1-O6 (Å)
$Li_{3.5}IrO_4$	2.00919	2.00091	2.13089	2.01611	2.05869	2.08554
Li_4IrO_4	2.01128	2.00733	2.10929	2.01545	2.07146	2.13177
$Li_{4.5}IrO_4$	2.00145	2.01868	2.10682	2.08573	2.09645	2.14617
Li_5IrO_4	2.13212	2.13231	2.13994	2.15297	2.15310	2.14000
	Ir2-O2 (Å)	Ir2-O4 (Å)	Ir2-O5 (Å)	Ir2-O6 (Å)	Ir2-O8 (Å)	Ir2-O7 (Å)
$Li_{3.5}IrO_4$	1.99073	1.89885	2.04035	2.06891	2.00568	2.05986
Li_4IrO_4	1.97220	2.03416	2.13832	2.08855	2.01619	2.11374
$Li_{4.5}IrO_4$	2.11393	2.12556	2.15724	2.16292	2.13903	2.10440
Li_5IrO_4	2.13223	2.13223	2.14006	2.15304	2.15303	2.13989

Table S1-2. Ir and O atomic population (e-) and Bader charges								
	$Li_{3.5}IrO_4$		Li_4IrO_4		$Li_{4.5}IrO_4$		Li_5IrO_4	
	Atom net population	Bader Charge	Atom net population	Bader Charge	Atom net population	Bader Charge	Atom net population	Bader Charge
Ir1	7.542	1.458	7.588	1.412	7.634	1.366	7.954	1.046
Ir2	7.339	1.661	7.568	1.432	7.918	1.082	7.956	1.044
O1	7.263	-1.263	7.272	-1.272	7.270	-1.270	7.383	-1.383
O2	7.195	-1.195	7.203	-1.203	7.340	-1.340	7.381	-1.381
O3	7.253	-1.253	7.278	-1.278	7.270	-1.270	7.383	-1.383
O4	7.094	-1.094	7.312	-1.312	7.367	-1.367	7.380	-1.380
O5	7.057	-1.057	7.138	-1.138	7.193	-1.193	7.220	-1.220
O6	7.079	-1.079	7.159	-1.159	7.208	-1.208	7.223	-1.223
O7	7.031	-1.031	7.123	-1.123	7.160	-1.160	7.222	-1.222
O8	7.079	-1.079	7.091	-1.091	7.159	-1.159	7.222	-1.222

Bibliography

1. Dronskowski, R.; Bloechl, P. E., Crystal orbital Hamilton populations (COHP): energy-resolved visualization of chemical bonding in solids based on density-functional calculations. *J. Phys. Chem.* **1993,** 97, (33), 8617-8624.